Experimental insights on the stability of core-shell structure in single Sn/SnOx spherical nanoparticles during room temperature oxidation

M. Heggen[1], J.E. Martinez Medina[2,3], A.M. Philippe[2], E. Barborini[2]*

[1]Ernst Ruska-Centre for Microscopy and Spectroscopy with Electrons (ER-C), Forschungszentrum Jülich GmbH, Jülich, Germany

[2]Luxembourg Institute of Science and Technology (LIST), Belvaux, Luxembourg

[3]Department of Physics and Materials Science, University of Luxembourg, Esch-Sur-Alzette, Luxembourg

*Corresponding author: Emanuele Barborini, Luxembourg Institute of Science and Technology (LIST), 41 Rue du Brill, L-4422 Belvaux, Luxembourg, emanuele.barborini@list.lu

Abstract

Experimental insights on the dimensions and stability of Sn/SnOx core-shell structures formed by oxidation of tin nanoparticle surface at room temperature are presented. Oxidation completes within a few minutes, ruling out slow dynamics, and leads to oxide shells exhibiting a constant thickness of 4.6 ± 0.7 nm in all nanoparticles larger than approximately 17 nm. This is consistent with the self-limiting nature of the Cabrera-Mott oxidation model based on inward and outward drift of oxygen anions and metallic cations respectively. Since particles smaller than 17 nm range do not exhibit any core-shell structure and appear fully oxidized, we suggest that 8 nm is a critical dimension for the stability of the metallic tin core. *In-situ* evolution of core-shell structures under electron beam irradiation appears to further support this conclusion. In addition to surface curvature, size-related thermodynamic properties of tin may provide key insights into understanding these observations.

Keywords

Tin oxides; Nanoparticles; Oxidation; Core-shell; Transmission Electron Microscopy; Cabrera-Mott

Introduction

Cabrera-Mott theory describes the growth of the oxide layer onto a metal surface as a process where quantum tunnelling of electrons from the Fermi level of the metal to the acceptor levels of oxygen adsorbates, through the sprout oxide layer, creates an intense electric field across the oxide, which promotes outwards migration of metal cations and inward of oxygen anions **[1,2]**. Fast at the beginning, ions migration slows down as the oxide layer grows and the electric field across it weakens. Cabrera-Mott theory accounts for this “self-limiting” mechanism proposing that the oxide thickness has logarithmic dependence on time for given conditions of temperature and oxygen concentration. Even if in principle this suggests that the oxide layer continuously grows with time, practically this means that a limit thickness does exist, especially at room temperature **[3,4]**. Despite its unquestionable importance, the original model remains a “global” description that does not consider neither the very early stages of oxide formation onto the metal surface, , nor geometrical and topological aspects such as the local curvature and the nanoscale surface texture. In this regard, a major example of system where refinement of Cabrera-Mott theory is necessary is represented by metallic nanoparticles having dimension in the range from few nanometres to few tens of nanometres **[5-9]**. For example, Ermoline et al. investigated oxidation-related volume changes in the configuration where a spherical metallic particle gets oxidized by a surrounding oxidizing compound, unveiling that models require significant corrections for nanoparticles dimensions below 10 nm **[7]**. In their work, comparison with experimental data was done for aluminium, nevertheless we will see in the following that dimension below 10 nm are critical for tin too.

In the last decades it has been experimentally observed an articulated phenomenology in structures resulting from oxidation of metallic nanoparticles and nanostructures. If inward drift of oxygen anions is faster than

outward drift of metal cations, oxidation can proceed till the whole metallic particle becomes a compact oxide particle. On the contrary, a faster outward drift of metal cations will result in creating empty volumes (voids) in the core of the metal particle, eventually leading to hollow oxide structures (Kirkendall effect). In the first scenario, if the size of the particle is "not too small" or the temperature at which oxidation occurs is "not too high", the self-limiting character of Cabrera-Mott mechanism generates core-shell structures, where a metallic core is surrounded by an oxide shell with proper thickness **[10-16]**.

With a bulk melting point as low as 232°C, which further decreases upon particle dimension and suddenly drops for particles below 10 nm, and a latent heat of fusion showing the same behaviour **[17,18]**, tin is of particular interest in this context. In fact, ion migration is expected to be facilitated and liquid-solid phase transition phenomena of the metal may coexist with oxidation process and be even triggered by the energy release of the latter. Room temperature oxidation of tin nanoparticles is known to generate core-shell structures, having body-centred tetragonal β-Sn as metallic core. However, studies aiming at describing the details of such Sn/SnO_x core-shell structure, particularly the nature of the oxide shell, do not offer a unique picture. For example, based on high-resolution transmission electron microscopy and X-ray photoelectron spectroscopy, Sutter et al. suggest amorphous SnO shells **[14]**, while other authors claim for SnO_2 or graded $SnO\text{-}SnO_2$ structures **[19-21]**. Very recently we showed that intermediate oxide Sn_3O_4, beside SnO and SnO_2, can be observed in nanostructured Sn films obtained by soft-assembling of Sn nanoparticles followed by room temperature oxidation, and we proposed a compositional gradient with increasing O/Sn ratio $Sn\text{-}SnO\text{-}Sn_3O_4\text{-}SnO_2$ as characterizing the material structure from the metal core to topmost shell layer **[22]**.

Understanding the Sn/SnOx core-shell system is crucial due to their potential applications in various technological fields. These include for example chemoresistive gas sensing, where tin oxide is one of the most widely used sensing materials on which nanostructuration favours the interaction with airborne chemical compounds **[23]**, and lithium-ion (and sodium-ion) batteries, where tin is being suggested as possible anode **[24]**. In respect to the last, it is worth noting that nowadays limitations of tin anodes, such as performance drift due to cyclic volume changes during Li ions incorporation and release, might be addressed effectively through nanostructuring **[25]**.

As schematically shown in **Fig. 1**, in this article we report the study of single Sn/SnOx core-shell spherical structures obtained by room-temperature oxidation of metallic Sn nanoparticles with size 2-40 nm. Samples were produced by Supersonic Cluster Beam Deposition (SCBD), a gas-phase deposition method generating metallic nanoparticles from a high-purity solid metal precursor and depositing them in high-vacuum conditions **[26,27]**. Through High-Resolution Transmission Electron Microscopy (HR-TEM), the diameter of metallic cores and the thickness of oxide shells were evaluated for particle ensembles subjected to exposure to air as short as 10 minutes and as long as 6 months. Fast Fourier Transform (FFT) analysis of lattice planes of metallic core provides information about core crystalline nature, while Electron Energy Loss Spectra (EELS) with sub-nanometric lateral resolution were acquired on single nanoparticles focusing on the shell, on the shell-core interface, and on the core. Finally, core-shell structure evolution upon *in-situ* irradiation with TEM electron beam was investigated.

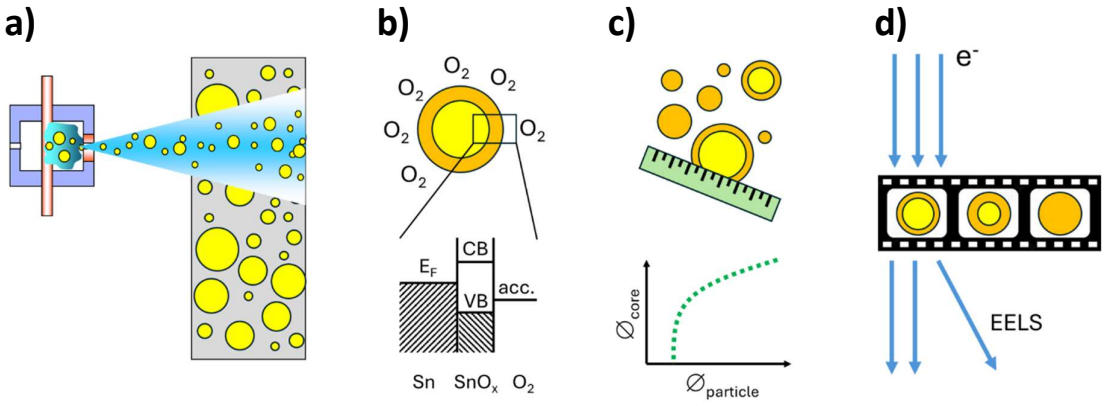

Figure 1. Scheme of the research content of the article. **a)** Sn nanoparticles were produced in UHV by Supersonic Cluster Beam Deposition. **b)** Air exposure at room temperature induced surface oxidation according to Cabrera-Mott mechanism, based on electron tunnelling from Fermi level of Sn (E_F) to oxygen acceptor levels (acc.). **c)** Diameters of

particles and of their metallic cores were correlated. **d)** Electron Energy Loss Spectra (EELS) and evolution of core-shell structures upon e-beam irradiation were finally investigated.

Experimental Methods

Samples of metallic Sn nanoparticles were prepared by a SCBD deposition apparatus equipped with a Pulsed Microplasma Cluster Source (PMCS) **[28,29]**. PMCS was backed with 40 bar neon gas (Messer, 6.0 purity) and loaded with 3 mm diam. tin rod (Goodfellow, 99.99% purity). Discharge voltage, current pulse duration and repetition rate were 500 V, 30 µs and 4 Hz, respectively. It has been observed that these process parameters avoid major deformations of the tin electrode ensuring PMCS stable operation over hours deposition time. Base pressure in deposition chamber was < 1×10^{-7} mbar. Holey carbon coated TEM copper grids (200 mesh, Agar Scientific) were used as substrates and directly exposed to the cluster beam. Beam intensity was monitored during samples preparation through a quartz crystal microbalance (QCM, Inficon SQM-160) and the duration of the deposition was established accordingly, aiming at obtaining samples where the majority of Sn nanoparticles are well separated from each other. This is a delicate aspect of sample preparation due to coalescence phenomena affecting Sn nanoparticles deposited by SCBD when getting in touch, even at room temperature **[30]**.

After deposition, tin nanoparticles were exposed to air at room temperature to induce oxidation and formation of core-shell structures. Two groups of samples were analysed by High-Resolution Transmission Electron Microscopy (HR-TEM): one immediately after venting the deposition chamber, whose total exposure time to air can be estimated around 10 minutes, one after six months of exposure to air; in both cases, at room temperature. HR-TEM instruments used are a JEOL JEM-F200 cold FEG microscope operating at an acceleration voltage of 200 kV and a FEI Titan 80-300 kV instrument, equipped with a spherical-aberration corrector for the objective lens (CEOS Company), operating at 300 kV. High-resolution Scanning Transmission Electron Microscopy (HR-STEM) analysis was conducted on a Hitachi HF5000 microscope and an FEI TITAN 80-200 ChemiSTEM, both equipped with spherical-aberration probe correctors, operating at 200 kV. Electron Energy Loss Spectroscopy (EELS) was performed using a Enfinium 977 ER spectrometer (Gatan Inc., Pleasanton, CA, USA). The EEL spectra were collected with a convergence semi-angle of 25 mrad and a collection semi-angle of 29 mrad at a dispersion of 0.1 eV/channel. The energy resolution is 1.25 eV according to full width at half maximum of the zero-loss peak.

Results and Discussion

The size distribution of Sn nanoparticles of the present work has been previously discussed in **[30]**, where a log-normal distribution for low-coverage samples featuring mean at 7 nm and log standard deviation of 0.48 nm is reported. Log-normal size distribution is in line with the outcomes of gas-phase aggregation processes **[31,32]**, as taking place in PMCS. Based on HR-TEM images, several isolated spherical/spheroidal nanoparticles showing core-shell structure were shortlisted and their external diameters as well as the diameter of their metallic cores were measured through ImageJ software. A pair of measurements for each diameter was collected in orthogonal directions, reporting the final value as the average of the two measurements. **Fig. 2** shows examples of HR-TEM images subjected to measurement and the scatter graph of core diameters vs. nanoparticle diameters, where datapoints colour distinguishes the nanoparticle group subjected to 10 minutes exposure to air (red) and the group subjected to 6 months exposure (blue). Data distribution shows no substantial difference between nanoparticles groups, which remarkably suggests that oxidation process and formation of core-shell structures get completed in a time scale of the order of minutes. This is at odd with respect to the results presented by other authors, where the thickness of the tin oxide shell is observed to regularly increase in time based on characterization of samples after 24 hours of air exposure, 10 days, and 60 days **[14]**. For a given nanoparticles dimension, this raises questions about other specificities of the samples undergoing oxidation and ultimately about how “overlapped”, in terms of overall characteristics, samples from different deposition methods can be.

The substantial overlap of datapoints from the two groups justifies a unique linear fitting (black dashed line), which returns $d_c = 1.0 \times d_{NP} - 9.35$ [nm], d_c and d_{NP} being the metallic core diameter and the nanoparticle diameter, respectively. As the oxide shell thickness is $(d_{NP} - d_c)/2$, the value 1.0 of the slope of the fitting line

brings to the conclusion that shell thickness is constant, i.e. it does not depend on nanoparticle size (in this range of sizes). This allows averaging the oxide thickness values $(d_{NP} - d_c)/2$ from the entire nanoparticles' dataset, which returns 4.6 ± 0.7 nm.

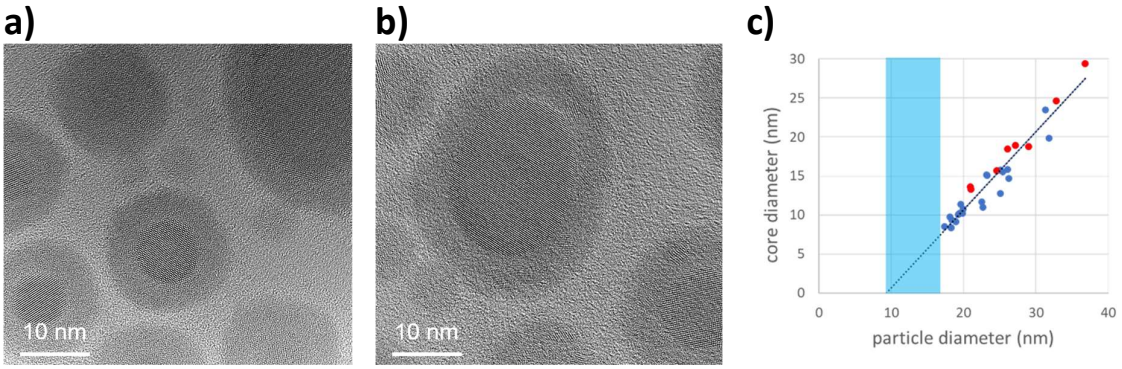

Figure 2. **a-b)** Examples of HR-TEM images showing spherical/spheroidal core-shell nanoparticles used for diameters analysis. **c)** Scatter graph of core diameters vs. nanoparticle diameters, where red points refer to nanoparticles subjected to 10 min exposure to air and blue points to nanoparticles subjected to 6 months exposure. Black dashed line extrapolates linear fitting of the entire dataset to $d_c = 0$. Cyan area emphasizes the lack of nanoparticles with core-shell structures smaller than about 17 nm although in principle they could exist down to about 9 nm.

Although in principle this shell thickness would allow the existence of core-shell particles with diameter down to about 9 nm, it was not possible to observe any core-shell particle smaller than about 17 nm: all nanoparticles smaller than about 17 nm show uniform contrast across their volume with a degree of grey similar to the one of the shell in core-shell nanoparticles and no lattice structures, suggesting they are fully oxidized and amorphous. This confirms that inward drift of oxygen anions is faster than outward drift of tin cations and suggests that a sudden change in the behaviour of the rate limiting specie, i.e. oxygen, takes place once core size approaches the dimension of 8 nm. We propose that such dimension might represent a critical size below which the metallic Sn core cannot survive the oxidation process, even at room temperature.

It is known that geometrical arguments could support this: due to the curvature of metallic core surface at these dimensions, Cabrera-Mott electric field is pushed at intensities such that "self-limiting" characteristic fails, and ion drift proceeds disruptively. Sutter et al. investigated the role of surface curvature of metallic core on oxidation enhancement in the case of indium and tin, showing agreement between experimental data and Cabrera-Mott model predictions for spherically symmetric electric field **[12,14]**. They highlight the fact that in spherical geometry the electric field across the oxide layer is inhomogeneous, presenting a magnitude at the surface of the metal core given by $E = -\frac{V_M}{L}\left(\frac{R}{R-L}\right)$, where R, L, and V_M are the nanoparticle radius, the thickness of the oxide layer, and the Mott potential, respectively, making therefore E diverging for $R \to L^+$. However, their results point out that the oxidation proceeds with slow dynamics since the three cohorts of nanoparticles exposed to 24 hours, 10 days, and 60 days of air exposure, show increasing thickness of the oxide shell. Moreover, regarding the existence of a critical size, this clearly appears in their data only for nanoparticles with the longer air exposure, i.e. 60 days, where the size of the particles showing "over-oxidation" phenomenon is around 20 nm. Since the thickness of the oxide layer of this cohort just above 20 nm size is 5-6 nm, it turns out that the metallic core of particles undergoing "over-oxidation" has a diameter of 8-10 nm, in line with our observations. We might conclude that, in our case, after 10 minutes of air exposure we observe the phenomenon described by Sutter et al. occurring after 60 days of air exposure. We propose that such remarkable time difference might be attributed to the nature of the oxide shell, which is claimed to be SnO in Sutter et al. work while it is has a graded SnO_2, Sn_3O_4, SnO, composition in our case **[22]**. Defects mobility and ion drift velocity within these oxide shell compositions might account for such different dynamics. An open question remains about the reason for such difference in shell composition and the role played in that by sample preparation methods.

In addition to geometrical arguments affecting Cabrera-Mott electric field, thermodynamics should also be considered in the picture. According to the Gibbs-Thomson equation and related discussions in Samsonov et al. **[18]**, the melting temperature T_m of metallic nanoparticles decreases with the decreasing of the dimension of the particles, showing a linear trend with respect to reciprocal radius of the particle $T_m \sim R^{-1}$. This causes a

sudden drop of T_m when dimensions reach few nanometres, as experimentally confirmed through scanning nanocalorimetry for the case of tin by Lai et al. **[17]**. Considering the adiabatic approximation justified by the fast oxidation dynamics observed in our study, we suggest that the heat release by oxidation might trigger phase transitions that favour ion mobility and "avalanche" completion of oxidation of Sn particles in the above size range. Additional clues of this phenomenon are discussed in the final part of the article.

In HR-TEM images, all nanoparticle cores -when present- show a well-defined lattice structure. Exploiting Selected Area Electron Diffraction (SAED) and X-ray Diffraction (XRD), we already demonstrated the presence of crystalline metallic tetragonal β-Sn phase in samples constituted by large cohorts of isolated Sn nanoparticles and in nanostructured films obtained by Sn nanoparticles assembling **[22]**. In the present work we processed 30 HR-TEM images of single nanoparticles by Fast Fourier Transform (FFT) analysis, and we extracted reciprocal lattice data through DigitalMicrograph® software V3.60.4441.0 (Gatan Inc., Pleasanton, CA, USA). **Fig. 3** shows an example of an HR-TEM image used for FFT analysis, the related FFT image, and the statistic of the lattice spacing values extracted from the whole FFT analysis, where the intensities of the Fourier components are plotted vs. lattice spacing values. The weighted averages of spacing values of each accumulation groups of dots are represented by the orange dashed lines in **Fig. 3c** and are reported in **Table 1** together with the attributed crystalline plane and the reference spacing from bulk metallic β-Sn.

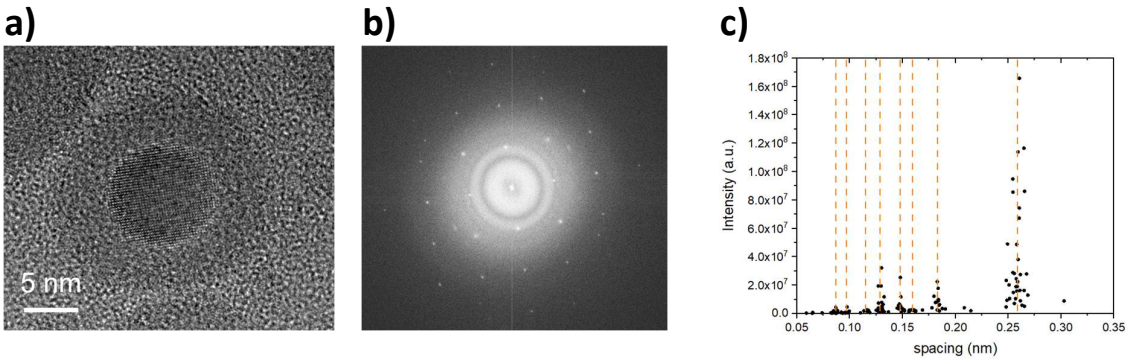

Figure 3. **a)** Example of an HR-TEM image and corresponding FFT analysis (**b)**. **c)** Statistic of the lattice spacing values extracted from FFT analysis on 30 nanoparticles, obtained by plotting the intensities of the Fourier components against lattice spacing values. Orange dashed lines are positioned along the weighted averages of spacing values of each accumulation groups of dots.

Table 1. Weighted averages of spacing values of **Fig. 3c**, attributed crystalline planes, and reference spacing from bulk metallic β-Sn.

d (nm)	Plane (hkl)	d_{bulk} (nm)
0.2600	(210)	0.261
0.1831	(310)	0.184
0.1597	(301)	0.166
0.1481	(112)	0.148
0.1295	(411)	0.129
0.1164	(312)	0.120
0.0973	(501)	0.109
0.0864	(442)	0.086

Electron Energy Loss Spectroscopy (EELS) is known to provide information about materials electronic structure at volume level with sub-nanometre lateral resolution if coupled to TEM. As oxygen 2p orbitals form bonding and antibonding bands with tin 5s and 5p orbitals whose empty states are mapped by oxygen K-edge absorption features, EELS at oxygen K-edge energy is of particular interest to distinguish among the various tin oxide species. In this respect, oxygen K-edge spectrum of stannic oxide SnO_2 is known to be characterized by a first peak and by a second broader structure, where the former refers to O 2sp antibonding σ* states hybridized with the empty Sn 5s states while the latter refers to O 2sp states and O 2p states hybridized with Sn 5p states. In the case of stannous oxide SnO, hybridization of oxygen states involves Sn 5p and 4d states **[33]**.

Moreno et al. carried out EELS studies supported by *ab-initio* calculations on commercial powders of SnO and SnO_2 aiming at distinguishing spectral fingerprints of the two main tin oxides, as well as of possible "intermediate oxides" Sn_xO_y ($0.5 < x/y < 1$) **[34,35]**. In fact, due to sensitivity to nearest-neighbour coordination, EELS features differ in SnO and SnO_2, as oxygen anions are surrounded by a regular tetrahedron of tin cations in SnO while they are in a triangular coordination in SnO_2. Main EELS spectral structures in tin oxides are those related to oxygen K-edge and tin M_4 - M_5 delayed edges, at energy loss values in the range 530-540 eV and 485-495 eV, respectively. In particular, oxygen-K shows a twofold peak structure whose energy difference depends on oxide nature, whether SnO or SnO_2, as also reported by Zhao et al. **[36]**.

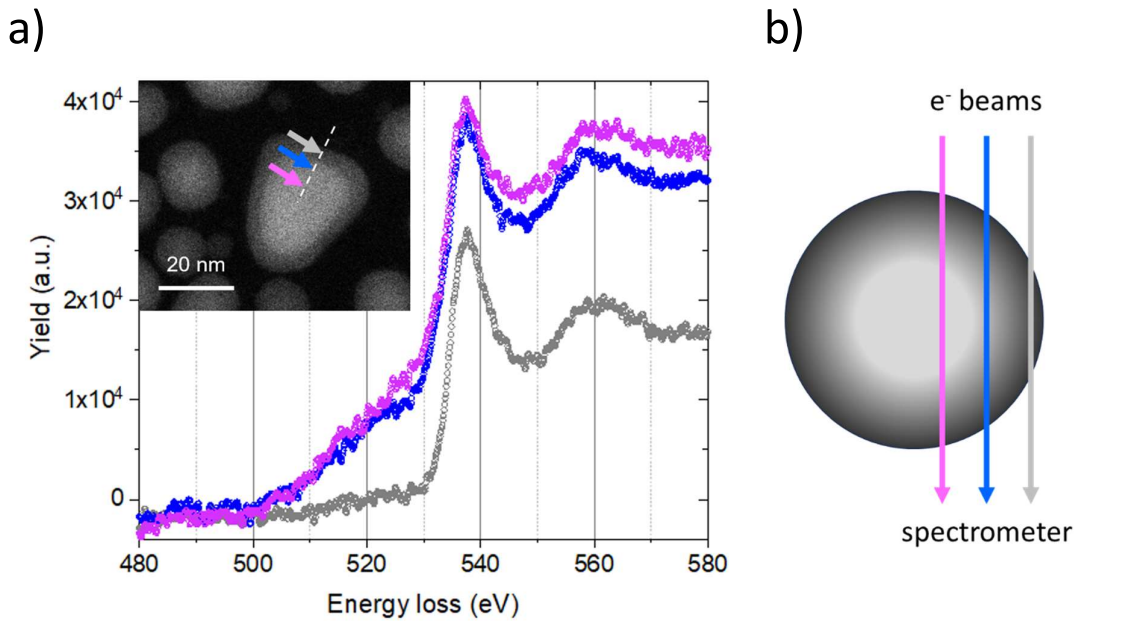

Figure 4. **a)** EELS spectra from different regions of a single core-shell nanoparticle: core (purple), shell (grey), and in between region (blue), as indicated in the inset, where the side of the white square is 50 nm. Peak at energy loss values 530-545 eV is attributed to oxygen K-edge, which overlaps to tin M4 - M5 delayed edges constituting the background signal on the rise at around 500 eV. Except for the rise of tin-related background in blue and purple spectra, no major differences can be highlighted. We suppose that, due to spherical geometry and similar dimensions of shells and cores, EELS spectra collected at different radial positions are the overlap of contributions of different stoichiometries in similar amount, as schematically shown in **b)**.

We analysed single core-shell nanoparticles by EELS coupled to HR-TEM, probing regions located in the shell, in the core, and roughly in between. **Fig. 4** shows a typical example of EELS spectra and the related positions of spectra acquisition in the core-shell nanoparticle. Baseline has been fitted with a simple power-law curve and subtracted to raw data. Tin M_4 - M_5 delayed edges at 485-495 eV are barely visible above noise level. oxygen K-edge structure at energy loss values 530-545 eV is clearly visible, overlapped to the tail of tin M_4 - M_5 delayed edges, which constitutes a sort of background. In each one of the measured positions, oxygen K-edge does not show the expected spectral components described in the literature and distinguishing among tin oxides. In addition, no major differences are observed among spectra collected at the three radial positions highlighted in **Fig. 4**, except for the relative increase of tin-related background when core position (purple) and intermediate position (blue) are probed, with respect to shell one (grey) where oxygen prevails. Even if we already demonstrated the presence of SnO_2, SnO, as well as Sn_3O_4 in nanogranular tin oxide films obtained by the soft assembling of nanoparticles similar to the ones of the present study and we proposed a radial distribution of the various stoichiometries **[22]**, we were not able to confirm here the same on single nanoparticles. As schematically shown in **Fig. 4b**, spherical geometry and similar dimensions of shells and cores, allegedly cause EELS spectra collected at different radial positions to be the overlap of contributions of different stoichiometries in similar amount.

Aiming at highlight phase-related density distribution in core-shell structures, nanoparticles were further investigated using high-angle annular dark field (HAADF) STEM, as this imaging technique provides contrast

related to the local average atomic number Z. In order to achieve "Z-Contrast" conditions, a probe semi-angle of 32 mrad and an inner collection semi-angle of the detector of 60 mrad were used. At an electron beam current of about 130 pA, it is observed that structural transformations occur within a timescale of seconds. In particular, the bright contrast crystalline core shrinks and finally disappears and at the same time the dark-contrast shell expands inwards. **Fig. 5** shows a sequence of images of the same sample region, where this transformation is observed occurring in many nanoparticles. As additional oxygen is not provided, we propose that electron beam irradiation induces sample heating which in turns favours inward oxygen diffusion driven by concentration gradient. In this scenario, a sub-stoichiometric oxide is supposed to form in the entire nanoparticle volume at the end of the process. The O/Sn molar ratio of a particle at the end of such oxygen diffusion process can be estimated assuming that oxygen comes from the initial SnO_2 shell of constant thickness of 4.6 nm, while tin comes from both the SnO_2 shell and the metallic core. Through simple calculations, it turns out that O/Sn = 1.8, 1.6, 1.4 in particles of 16, 20, and 25 nm diameter, respectively. This accounts for the final grey shade of the whole nanoparticle to appear similar to the one of the shells at the starting of the process.

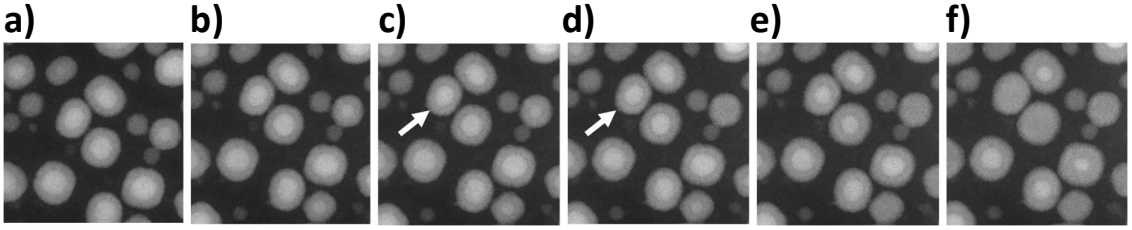

Figure 5. **a-f)** HAADF-STEM image series showing structural transformations within Sn/SnOx nanoparticles. Images side is 80 nm, elapsed time between frames is 26 s. Framed area in **a)** is slightly shifted upward with respect to objects position. Arrows in **c-d** highlight the particle enlarged in **Fig. 6 a-b**.

Interestingly, we observe the presence of a thin dark ring between core and shell as the inward growth of the shell progresses. In terms of image contrast, this observation suggests that inward growth of the oxide shell has a forefront whose average density and/or atomic number Z is much lower than both the metallic core as well as the oxide shell. Since $Z_{Tin} \gg Z_{Oxygen}$, we argue that such low-Z contrast may be ascribable to the diffusion and accumulation of Sn vacancies at the surface of the metallic core, which favour the subsequent reaction with O atoms diffusing from the shell. Vacancy migration might be promoted by the specific thermodynamic properties of tin **[17,18]**.

As shown in **Fig. 6**, at the very final stages of this process, just before metallic cores become indistinguishable from the shells, we observed the disappearance of lattice structure in the cores though their image contrast is still different from shell one. This might suggest that metallic cores undergo a sudden phase transition from crystalline solid to liquid, as previously commented, with the difference that in this case the energy is provided to the system through the electron beams. Interestingly, the dimension of the metallic cores at this stage is around 8 nm, once more suggesting this size to be a sort of critical size for metallic tin core. The example of **Fig. 6 a-b** shows the phenomenon in two consecutive frames, separated by 26 s time. **Fig. 6 c-d** show the disappearing of the lattice structure during the image scan acquisition (black arrows). The lattice image contrast disappears within a few horizontal scan lines, i.e. on a timescale as short as around 100 ms.

a) **b)**

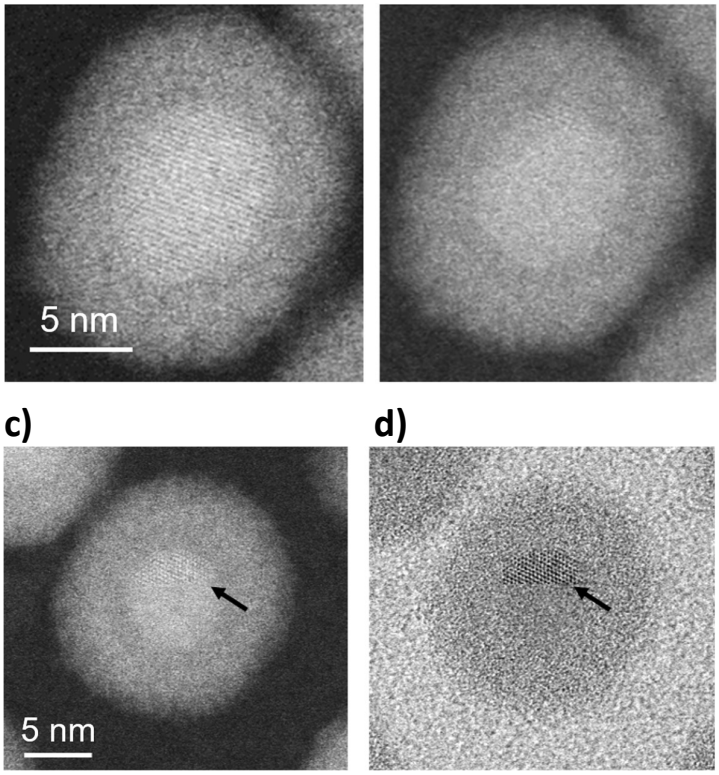

Figure 6. **a-b)** Consecutive frames of an HAADF-STEM image series of the same core-shell nanoparticle during e-beam irradiation, showing the sudden disappearing of the crystalline lattice structure in the metallic Sn core. As the image contrast of the core in the second frame is still different (lighter) from the one of the oxide shell, we argue that a phase transition from crystalline solid to liquid is taking place in metallic tin core. The images refer to the particle pointed by the arrows in **Fig. 5**. **c-d)** Corresponding HAADF and bright-field STEM during e-beam irradiation, showing the sudden disappearing of the crystalline lattice structure during image acquisition (see image contrast change in the bright field image, black arrow) in the metallic Sn core. Again, the image contrast of the core in the corresponding HAADF-STEM image is still different (lighter) from the one of the oxide shell.

Conclusions

We studied room-temperature oxidation of Sn nanoparticles with dimension from few nanometres to few tens of nanometres by High Resolution Transmission Electron Microscopy. Supersonic Cluster Beam Deposition was used for sample production as the method operates on a high-purity metallic precursor and in high-vacuum conditions, offering optimal prerequisites in respect to samples contamination issues.

The absence of differences in samples undergoing 10 minutes oxidation and six-month oxidation suggests that fast dynamics govern the phenomenon. This contrasts with other studies reported in the literature, where the evolution of the core-shell structures is observed on a much longer timescale. We measured the thickness of the oxide shell to have a constant value of 4.6 ± 0.7 nm for nanoparticles larger than 17 nm, while below this size no core-shell nanoparticle is observed. This suggests that, as soon as the dimension of the metallic core is approaching 8 nm, the "self-limiting" character of Cabrera-Mott mechanism is no more in place and oxidation proceeds till the whole metallic volume gets oxidized. The dimension of about 8 nm of the metallic core might represents a critical size for Sn oxidation ascribable to solid-to-liquid phase transitions triggered by size-depending Sn melting temperature. The sudden disappearing of lattice structure in Sn cores during *in-situ* e-beam irradiation when cores have about 8 nm size further corroborate the above. Unveiled during STEM imaging with long exposure to the electron beam, the presence of a thin layer with average atomic number

$Z \ll Z_{Tin}$ between the inward growing oxide shell and the shrinking metallic core suggests the accumulation of Sn vacancies at the surface of the metallic core, which favours the proceeding of inward oxidation.

We are confident that the experimental outcomes reported here may provide useful elements for the refinement of models describing room temperature oxidation of nanoparticles. We acknowledge the value of these results also for the applicative contexts where Sn/SnOx nanostructured films can be exploited. This holds in particular for Sn-based anodes in lithium-ion batteries, where nanostructuring might accommodate the cyclic changes of volume due to Li ions incorporation and release and mitigate the performance drift affecting devices exploiting compact films.

Acknowledgments

This work is supported by the Luxembourg National Research Fund (FNR), CLASMARTS project (C19/MS/13685974), and by SNOX project (ER-C E-002).

Conflicts of Interest

The authors declare no conflict of interest.

References

[1] N. Cabrera and N.F. Mott, Theory of the oxidation of metals, Reports on Progress in Physics 12, 163 (1949).

[2] A.T. Fromhold and E.A. Cook, Kinetics of Oxide Film Growth on Metal Crystals: Thermal Electron Emission and Ionic Diffusion, Physical Review 158, 600–612 (1967).

[3] N. Cai, G. Zhou, K. Müller and D.E. Starr, Tuning the Limiting Thickness of a Thin Oxide Layer on Al(111) with Oxygen Gas Pressure, Physical Review Letters 107, 035502 (2011). https://doi.org/10.1103/PhysRevLett.107.035502

[4] J. Gorobez, B. Maack and N. Nilius, Growth of Self-Passivating Oxide Layers on Aluminum—Pressure and Temperature Dependence, Physica Status Solidi B 2000559, 258 (2021). https://doi.org/10.1002/pssb.202000559

[5] P.A. Chernavskii, N.V. Peskov, A.V. Mugtasimov and V.V. Lunin, Oxidation of metal nanoparticles: Experiment and model, Russian Journal of Physical Chemistry B 1, 394–411 (2007). https://doi.org/10.1134/S1990793107040082

[6] V.P. Zhdanov and B. Kasemo, Cabrera–Mott kinetics of oxidation of nm-sized metal particles, Chemical Physics Letters 452, 4–6, 285-288 (2008). https://doi.org/10.1016/j.cplett.2008.01.006

[7] A. Ermoline and E.L. Dreizin, Equations for the Cabrera–Mott kinetics of oxidation for spherical nanoparticles, Chemical Physics Letters 505, 47–50 (2011). https://doi.org/10.1016/j.cplett.2011.02.022

[8] V.P. Zhdanov, Kinetic model of oxidation of metal nanoparticles: Cabrera-Mott and Kirkendall effects, Surface Science 684, 24-27 (2019). https://doi.org/10.1016/j.susc.2018.12.006

[9] X. Zhang, P. Zheng, Y. Ma, Y. Jiang and H. Li, Atomic-scale understanding of oxidation mechanisms of materials by computational approaches: A review, Materials & Design 217 (2022). https://doi.org/10.1016/j.matdes.2022.110605

[10] Y. Yin, R.M. Rioux, C.K. Erdonmez, S. Hughes, G.A. Somorjai and A.P. Alivisatos, Formation of Hollow Nanocrystals through the Nanoscale Kirkendall Effect, Science 304, 711–714 (2004). http://www.jstor.org/stable/3836820

[11] J.G. Railsback, A.C. Johnston-Peck, J. Wang and J.B. Tracy, Size-Dependent Nanoscale Kirkendall Effect During the Oxidation of Nickel Nanoparticles, ACS Nano 4, 4, 1913–1920 (2010). https://doi.org/10.1021/nn901736y

[12] E. Sutter and P. Sutter, Size-Dependent Room Temperature Oxidation of In Nanoparticles, The Journal of Physical Chemistry C 116, 38, 20574–20578 (2012). https://doi.org/10.1021/jp305806v

[13] Tae-Jong Yoon, H. Shao, R. Weissleder and H. Lee, Oxidation Kinetics and Magnetic Properties of Elemental Iron Nanoparticles, Particle and Particle Systems Characterization 30, 8, 667–671 (2013). https://doi.org/10.1002/ppsc.201300013

[14] E. Sutter, F. Ivars-Barcelo and P. Sutter, Size-Dependent Room Temperature Oxidation of Tin Particles, Particle Particle Systems Characterization 31, 879-885 (2014). https://doi.org/10.1002/ppsc.201300352

[15] B.D. Anderson and J.B. Tracy, Nanoparticle conversion chemistry: Kirkendall effect, galvanic exchange, and anion exchange, Nanoscale 6, 12195-12216 (2014). https://doi.org/10.1039/C4NR02025A

[16] P. García Acevedo, M.A. González Gómez, A. Arnosa Prieto, J.S. Garitaonandia, Y. Piñeiro and J. Rivas, Significant Surface Spin Effects and Exchange Bias in Iron Oxide-Based Hollow Magnetic Nanoparticles, Nanomaterials 12, 456 (2022). https://doi.org/10.3390/nano12030456

[17] S.L. Lai, J.Y. Guo, V. Petrova, G. Ramanath and L.H. Allen, Size-Dependent Melting Properties of Small Tin Particles: Nanocalorimetric Measurements, Physical Review Letters 77, 99 (1996). https://link.aps.org/doi/10.1103/PhysRevLett.77.99

[18] V.M. Samsonov, S.A. Vasilyev, K.K. Nebyvalova, I.V. Talyzin, N.Yu. Sdobnyakov, D.N. Sokolov and M.I. Alymov, Melting temperature and binding energy of metal nanoparticles: size dependences, interrelation between them, and some correlations with structural stability of nanoclusters, Journal of Nanoparticle Research 22, 247 (2020). https://doi.org/10.1007/s11051-020-04923-6

[19] Moo-Young Huh, Sun-Ho Kim, Jae-Pyoung Ahn, Jong-Ku Park and Byoung-Kee Kim, Oxidation of nanophase tin particles, Nanostructured Materials 11, 211-220 (1999). https://doi.org/10.1016/S0965-9773(99)00034-3

[20] K. Kravchyk, L. Protesescu, M.I. Bodnarchuk, F. Krumeich, M. Yarema, M.Walter, C. Guntlin and M.V. Kovalenko, Monodisperse and Inorganically Capped Sn and Sn/SnO2 Nanocrystals for High-Performance Li-Ion Battery Anodes, Journal of the American Chemical Society 135, 4199–4202 (2013). https://doi.org/10.1021/ja312604r

[21] N. Soulmi, D. Dambournet, C. Rizzi, J. Sirieix-Plénet, M. Duttine, A. Wattiaux, J. Swiatowska, O.J. Borkiewicz, H. Groult and L. Gaillon, Structural and Morphological Description of Sn/SnOx Core–Shell Nanoparticles Synthesized and Isolated from Ionic Liquid, Inorganic Chemistry 56, 10099–10106 (2017). http://dx.doi.org/10.1021/acs.inorgchem.7b01850

[22] J.E. Martinez Medina, A.M. Philippe, J. Guillot, C. Vergne, Y. Fleming and E. Barborini, Intermediate tin oxide in stable core-shell structures by room temperature oxidation of cluster-assembled nanostructured Sn films, Applied Surface Science 658, 159846 (2024). https://doi.org/10.1016/j.apsusc.2024.159846

[23] Yulin Kong, Yuxiu Li, Xiuxiu Cui, Linfeng Su, Dian Ma, Tingrun Lai, Lijia Yao, Xuechun Xiao and Yude Wang, SnO2 nanostructured materials used as gas sensors for the detection of hazardous and flammable gases: A review, Nano Materials Science 4, 4, 339-350 (2022). https://doi.org/10.1016/j.nanoms.2021.05.006

[24] Hui Liu, Shuzhong Wang, Junan Zhao, Baoquan Zhang, Lu Liu, Rui Bao and Zefeng Jing, Sn-based anode materials for lithium-ion batteries: From mechanism to modification, Journal of Energy Storage 80, 109862 (2024). https://doi.org/10.1016/j.est.2023.109862

[25] Haoyi Mou, Wei Xiao, Chang Miao, Rui Li and Liming Yu, Tin and Tin Compound Materials as Anodes in Lithium-Ion and Sodium-Ion Batteries: A Review, Frontiers in Chemistry 8, 141 (2020). https://doi.org/10.3389/fchem.2020.00141

[26] P. Milani, S. Iannotta, Cluster Beam Synthesis of Nanostructured Materials, Springer-Verlag, Berlin Heidelberg, 1999. https://doi.org/10.1007/978-3-642-59899-9

[27] E. Barborini, S. Vinati, Supersonic Cluster Beam Deposition for the integration of functional nanostructured films in devices, in: S. Krishnamoorthy, K. Iniewski (Eds.), Advances in Fabrication and

Investigation of Nanomaterials for Industrial Applications, Springer-Nature Switzerland AG (2024). https://doi.org/10.1007/978-3-031-42700-8_1

[28] E. Barborini, P. Piseri and P. Milani, A pulsed microplasma source of high intensity supersonic carbon cluster beams, Journal of Physics D: Applied Physics 32, L105 (1999). https://doi.org/10.1088/0022-3727/32/21/102

[29] J.E. Martinez Medina, D. Arl, A.M. Philippe, P. Grysan, J. Guillot, C. Vergne and E. Barborini, Nanostructured nickel films by supersonic cluster beam deposition: Morphology, oxidation, and clues of hollow structures by Kirkendall effect at room temperature, Vacuum 211, 111930 (2023). https://doi.org/10.1016/j.vacuum.2023.111930

[30] J.E. Martinez Medina, J. Polesel-Maris, A.M. Philippe, P. Grysan, N. Bousri, S. Girod and E. Barborini, The role of coalescence and ballistic growth on in-situ electrical conduction of cluster-assembled nanostructured Sn films, Applied Surface Science 664, 160268 (2024). https://doi.org/10.1016/j.apsusc.2024.160268

[31] C.G. Granqvist and R.A. Buhrman, Ultrafine metal particles, Journal of Applied Physics 47, 2200 (1976). https://doi.org/10.1063/1.322870

[32] R. Alayan, L. Arnaud, A. Bourgey, M. Broyer, E. Cottancin, J.R. Huntzinger, J. Lermé, J.L. Vialle, M. Pellarin and G. Guiraud, Application of a static quadrupole deviator to the deposition of size-selected cluster ions from a laser vaporization source, Review of Scientific Instruments 75 (7): 2461–2470 (2004). https://doi.org/10.1063/1.1764607

[33] F. Frati, Myrtille O.J.Y. Hunault and Frank M.F. de Groot, Oxygen K-edge X-ray Absorption Spectra, Chemical Reviews 120, 4056−4110 (2020). https://dx.doi.org/10.1021/acs.chemrev.9b00439?ref=pdf

[34] M.S. Moreno, R.F. Egerton and P.A. Midgley, Differentiation of tin oxides using electron energy-loss spectroscopy, Physical Review B 69, 233304 (2004). https://doi.org/10.1103/PhysRevB.69.233304

[35] M. S. Moreno, R. F. Egerton, J. J. Rehr and P. A. Midgley, Electronic structure of tin oxides by electron energy loss spectroscopy and real-space multiple scattering calculations, Physical Review B 71, 035103 (2005). https://doi.org/10.1103/PhysRevB.71.035103

[36] Q. Zhao, H. Lorenz, S. Turner, O.I. Lebedev, G. Van Tendeloo, C. Rameshan, B. Klötzer, J. Konzett and S. Penner, Catalytic characterization of pure SnO2 and GeO2 in methanol steam reforming, Applied Catalysis A: General 375, 2 (2010). https://doi.org/10.1016/j.apcata.2009.12.027